Evidence for a vestigial nematic state in the cuprate pseudogap phase

Sourin Mukhopadhyay[a,b], Rahul Sharma[b,c], Chung Koo Kim[c], Stephen D. Edkins[d], Mohammad H. Hamidian[e], Hiroshi Eisaki[f], Shin-ichi Uchida[f,g], Eun-Ah Kim[b], Michael J. Lawler[b], Andrew P. Mackenzie[h], J. C. Séamus Davis[i,j,1], and Kazuhiro Fujita[c]

[a]Department of Physics, Indian Institute of Space Science and Technology, 695547 Thiruvananthapuram, India; [b]Laboratory of Atomic and Solid State Physics, Department of Physics, Cornell University, Ithaca, NY 14853; [c]Condensed Matter Physics and Material Science Department, Brookhaven National Laboratory, Upton, NY 11973; [d]Department of Applied Physics, Stanford University, Stanford, CA 94305; [e]Department of Physics, Harvard University, Cambridge, MA 02138; [f]Nanoelectronics Research Institute, Institute of Advanced Industrial Science and Technology, 305-8568 Tsukuba, Ibaraki, Japan; [g]Department of Physics, University of Tokyo, 113-0033 Tokyo, Japan; [h]Max Planck Institute for Chemical Physics of Solids, D-01187 Dresden, Germany; [i]Department of Physics, University College Cork, T12 R5C Cork, Ireland; and [j]Clarendon Laboratory, University of Oxford, OX1 3PU Oxford, United Kingdom

Contributed by J. C. Séamus Davis, April 27, 2019 (sent for review December 21, 2018; reviewed by Riccardo Comin and Laimei Nie)

The CuO_2 antiferromagnetic insulator is transformed by hole-doping into an exotic quantum fluid usually referred to as the pseudogap (PG) phase. Its defining characteristic is a strong suppression of the electronic density-of-states $D(E)$ for energies $|E| < \Delta^*$, where Δ^* is the PG energy. Unanticipated broken-symmetry phases have been detected by a wide variety of techniques in the PG regime, most significantly a finite-Q density-wave (DW) state and a $Q = 0$ nematic (NE) state. Sublattice-phase-resolved imaging of electronic structure allows the doping and energy dependence of these distinct broken-symmetry states to be visualized simultaneously. Using this approach, we show that even though their reported ordering temperatures T_{DW} and T_{NE} are unrelated to each other, both the DW and NE states always exhibit their maximum spectral intensity at the same energy, and using independent measurements that this is the PG energy Δ^*. Moreover, no new energy-gap opening coincides with the appearance of the DW state (which should theoretically open an energy gap on the Fermi surface), while the observed PG opening coincides with the appearance of the NE state (which should theoretically be incapable of opening a Fermi-surface gap). We demonstrate how this perplexing phenomenology of thermal transitions and energy-gap opening at the breaking of two highly distinct symmetries may be understood as the natural consequence of a vestigial nematic state within the pseudogap phase of $Bi_2Sr_2CaCu_2O_8$.

cuprate | pseudogap | broken symmetry | density wave | vestigial nematic

The cuprate pseudogap energy Δ^* is defined to be the energy range within which significant $D(E)$ suppression occurs in underdoped cuprates (1, 2). Fig. 1*A* shows measured $D(E)$ for hole-density $P = 0.06$ in $Bi_2Sr_2CaCu_2O_{8+\delta}$, with arrow indicating a typical example of the feature in $D(E)$ that occurs at $E = \Delta^*$. Fig. 1*A* (*Inset*) shows the measured evolution of $D(E)$ and this signature of Δ^* with p. Fig. 1*B* shows the consequent doping dependence for this sequence of $Bi_2Sr_2CaCu_2O_{8+\delta}$ samples. This exemplifies the well-known correspondence (1) between $\Delta^*(p)$ and the temperature $T^*(p)$ at which the pseudogap phenomenology appears; both fall linearly with increasing p until reaching zero at approximately $p \approx 0.19$. In the last decade, extensive evidence has emerged for electronic symmetry breaking at or below $T^*(p)$ as shown schematically in Fig. 1*C*. For $T < T^*(p)$ and $p < p_C \approx 0.19$, two distinct classes of broken-symmetry states are widely reported. The first is a nematic state; it occurs at wavevector $\boldsymbol{Q} = 0$ and generally exhibits breaking of 90° rotational (C_4) symmetry (3–16); sometimes additional $\boldsymbol{Q} = 0$ broken symmetries are detected depending on the experimental technique. These phenomena have been reported using multiple techniques in $YBa_2Cu_3O_{7-x}$, $Bi_2Sr_2CaCu_2O_{8+x}$, $Bi_2Sr_2CuO_{6+x}$, and $HgBa_2CuO_{4+\delta}$, and are observed to occur below a characteristic temperature $T_{NE}(p)$, which appears to fall linearly with increasing p along the trajectory shown in Fig. 1*C*.

Already this is a conundrum: While the onset temperature $T_{NE}(p)$ of this broken symmetry tracks the temperature $T^*(p)$ at which pseudogap opens (Fig. 1*C*), within mean-field theory of electron fluids ordering at $\boldsymbol{Q} = 0$ it cannot open an energy gap on the Fermi surface. The second ordered state within the pseudogap phase breaks translational symmetry with axial wavevectors $\boldsymbol{Q} = (Q, 0); (0, Q)$ parallel to the CuO_2 axes (17–27). [Here we do not discuss the density-wave (DW) state generated by very high magnetic fields (26).] This zero-field DW state has been reported to occur in $La_{2-x}Ba_xCuO_4$, $YBa_2Cu_3O_{7-x}$, $Bi_2Sr_2CaCu_2O_{8+x}$, $Bi_2Sr_2CuO_{6+x}$, $HgBa_2CuO_{4+x}$, and $Ca_{2-x}Na_xCuO_2Cl_2$. In $YBa_2Cu_3O_{7-x}$, $Bi_2Sr_2CuO_{6+x}$, $Bi_2Sr_2CaCu_2O_{8+x}$, and $Ca_{2-x}Na_xCuO_2Cl_2$ samples, the DW exhibits a predominantly d-symmetry form factor (28–32). The DW phenomenology reveals a second puzzle: Although a DW with finite $\boldsymbol{Q}$ should open a mean-field energy gap spanning the Fermi energy (while folding the band structure due to the larger electronic unit cell), no energy gap is reported to open specifically at the cuprate DW onset temperature $T_{DW}(p)$. Moreover, $T_{DW}(p)$ is manifestly unrelated to the temperature $T^*(p)$ at which the pseudogap opens (Fig. 1*C*). Thus, the essence of the broken-symmetry riddle of

Significance

In the cuprate pseudogap phase, an energy gap of unknown mechanism opens, and both an electronic nematic phase (NE) and a density-wave (DW) phase appear. Perplexingly, the DW, which should generate an energy gap, appears without any new gap opening; and the NE, which should be incapable of opening an energy gap, emerges coincident with the pseudogap opening. Recently, however, it was demonstrated theoretically that a disordered unidirectional DW can generate a vestigial nematic (VN) phase. If the cuprate pseudogap phase were in such a VN state, the energy gap of the NE and DW should be identical to each other and to the pseudogap. We report discovery of such a phenomenology throughout the phase diagram of underdoped $Bi_2Sr_2CaCu_2O_8$.

Author contributions: S.M., C.K.K., S.D.E., M.H.H., and K.F. performed experiments; S.M., C.K.K., and K.F. analyzed data; E.-A.K. and M.J.L. provided theoretical guidance; H.E. and S.-i.U. synthesized the crystals; A.P.M., J.C.S.D., and K.F. supervised the project and wrote the paper with key contributions from S.M., R.S., C.K.K., S.D.E., and M.H.H.

Reviewers: R.C., Massachusetts Institute of Technology; and L.N., University of Chicago.

Conflict of interest statement: The authors declare a conflict of interest. H.E. and R.C. are coauthors on a 2015 article, "Symmetry of charge order in cuprates," *Nat. Mater.* **14**, 796–800 (2015).

[1]To whom correspondence may be addressed. Email: jcseamusdavis@gmail.com.

This article contains supporting information online at www.pnas.org/lookup/suppl/doi:10.1073/pnas.1821454116/-/DCSupplemental.

Published online June 3, 2019.

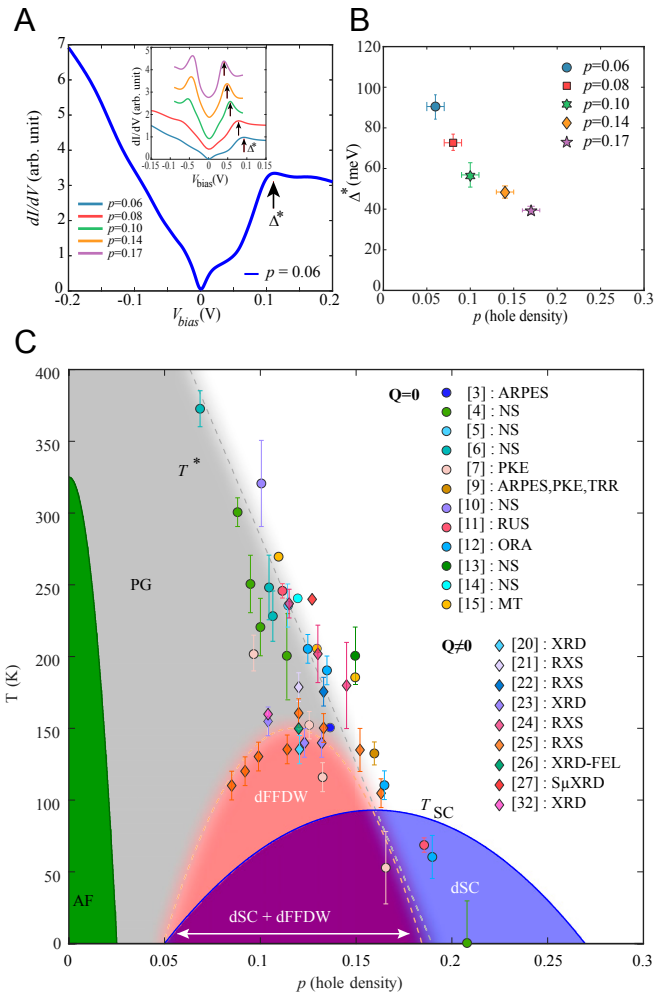

Fig. 1. Doping evolution of cuprate symmetry breaking and pseudogap. (*A*) Measured $D(E)$ at P = 0.06 and T = 2.2K in $Bi_2Sr_2CaCu_2O_{8+\delta}$. This $dI/dV(E=eV) \equiv g(E)$ curve is a typical tunneling spectrum of underdoped cuprates with empty-state density of states peak at energy Δ*. (*Inset*) Characteristic $g(E)$ for the range of $Bi_2Sr_2CaCu_2O_{8+\delta}$ samples (P = 0.06, 0.08, 0.10, 0.14, and 0.17) studied. The evolution of Δ*(p) is indicated by the black arrows. (*B*) Doping dependence of the measured average value of Δ* (P = 0.06, 0.08, 0.10, 0.14, and 0.17, respectively) from the set of $Bi_2Sr_2CaCu_2O_{8+\delta}$ samples studied. (*C*) Colored background represents schematic phase diagram of hole-doped CuO_2. Two classes of broken-symmetry states have been widely reported therein. The first indicated by circles occurs at wavevector $\boldsymbol{Q}=0$ and typically exhibits breaking of C_4 symmetry within the CuO_2 unit cell that appears at the pseudogap temperature scale T^*. The second state indicated by diamonds breaks translational symmetry with wavevector $\boldsymbol{Q}^{\boldsymbol{D}}=(Q,0);(0,Q)$ exhibiting a predominantly *d*FF, and often appears at a temperature scale far lower than T^*.

cuprates is that the DW state that could produce an energy gap in $D(E)$ is only detectable at temperatures $T_{DW}(p) << T^*(p)$ and without the opening of a new energy gap, while the nematic (NE) state that appears at the temperature $T_{NE}(p) \approx T^*(p)$ where the pseudogap opens should be incapable of opening a Fermi surface energy gap. No comprehensive explanation has been proposed to address these linked mysteries.

Symmetry Breaking in the Cuprate Pseudogap Regime

Both types of broken-symmetry states can be studied simultaneously in the same field of view (FOV) using high-resolution spectroscopic imaging scanning tunneling microscopy (SI-STM) (33). To do so, Fourier analysis of sublattice phase-resolved electronic structure imaging of the CuO_2 plane is required (8, 28–30). The tunnel-current $I(\boldsymbol{r},E)$ and tip-sample differential tunneling conductance $\frac{dI}{dV}(\boldsymbol{r},E=eV) \equiv g(\boldsymbol{r},E)$ are first measured

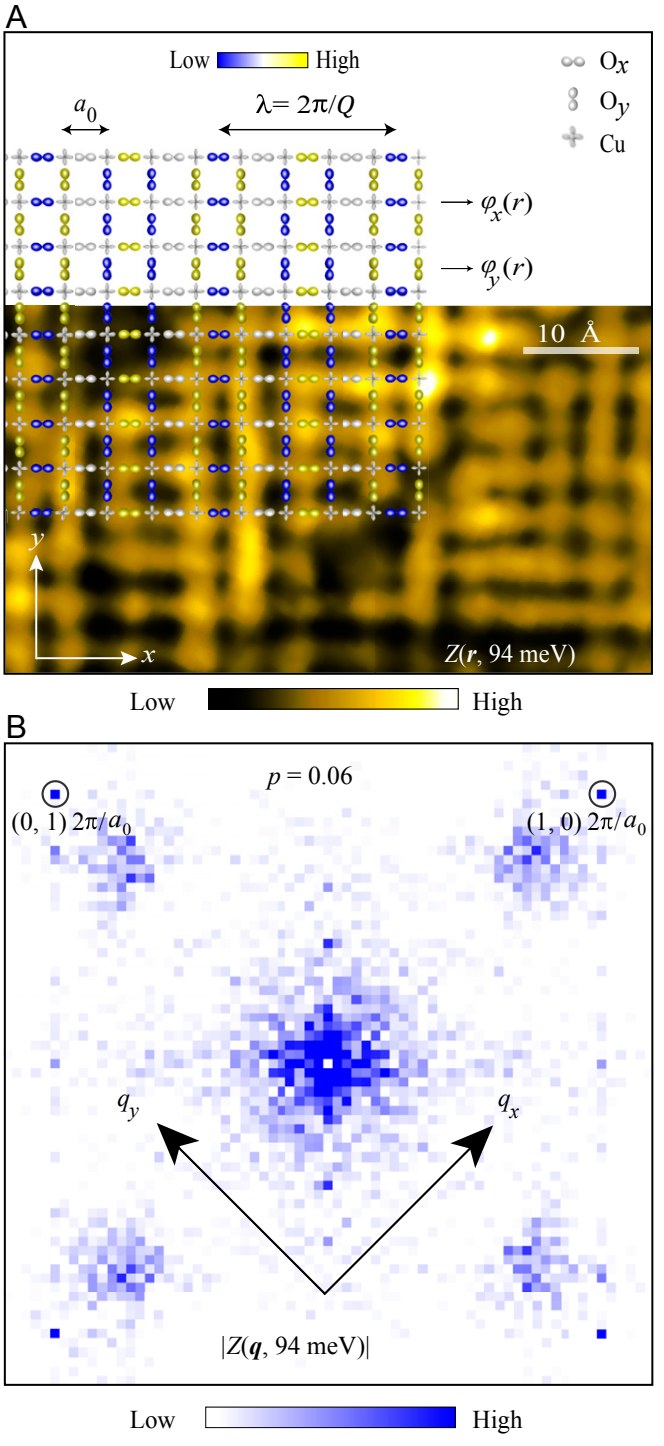

Fig. 2. $Q = 0$ and $Q \neq 0$ broken-symmetry states imaged simultaneously. (*A*) Real-space phase-resolved SI-STM image of dFF DW modulations in $Z(\boldsymbol{r}, E = 94$ meV) of a $Bi_2Sr_2CaCu_2O_{8+\delta}$ sample with $P = 0.06$ measured at T = 2.2 K. Transparent overlay shows the correspondences between the schematic dFF DW and the real-space phase-resolved electronic structure. Intraunit cell C_4 symmetry is broken in virtually every CuO_2 unit cell, and it is the modulation of this electronic inequivalence between O_x and O_y sites that generates the dFF DW state. (*B*) Typical Fourier transform image $Z(\boldsymbol{q},E)$ from underdoped $Bi_2Sr_2CaCu_2O_{8+\delta}$. Locations of the Bragg peaks $\boldsymbol{Q}_x^B$, $\boldsymbol{Q}_y^B$ are indicated by circles.

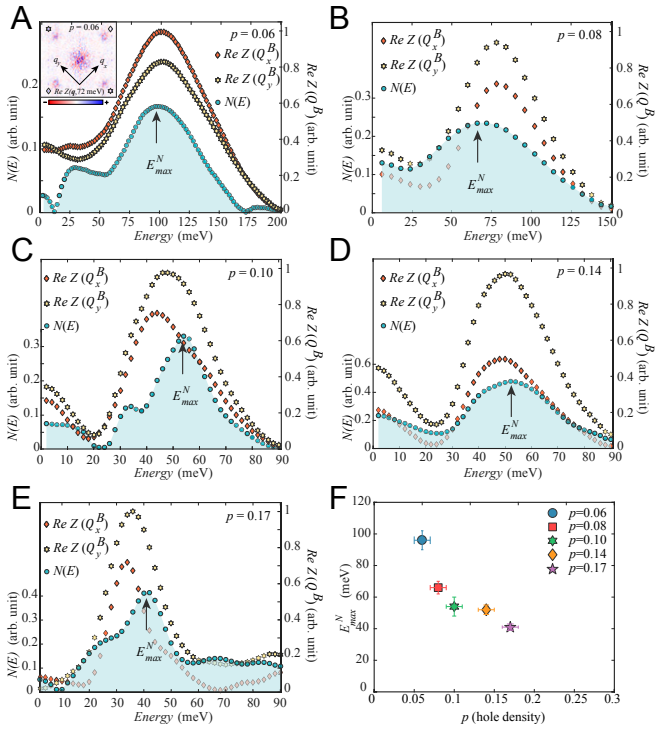

Fig. 3. Doping- and energy evolution of the $Q = 0$ broken-symmetry (NE) state. (*A*, *Inset*) Measured $ReZ(\boldsymbol{q}, E = 72\ \text{meV})$ for $Bi_2Sr_2CaCu_2O_{8+\delta}$ with $P = 0.06$ at $T = 2.2$ K. The magnitude of $N^Z(E) \equiv ReZ(\boldsymbol{Q}_y^B, E) - ReZ(\boldsymbol{Q}_x^B, E)$ is measured as the difference in real intensity of the two Bragg peaks at $\boldsymbol{Q}_x^B, \boldsymbol{Q}_y^B$ (indicated by diamond and star shapes). (*A–E*) Measured $ReZ(\boldsymbol{Q}_y^B, E), ReZ(\boldsymbol{Q}_x^B, E)$, and $N(E)$ versus hole density ($P = 0.06, 0.08, 0.10, 0.14$, and 0.17, respectively) in the $Bi_2Sr_2CaCu_2O_{8+\delta}$ samples at $T = 2.2$ K reported here. For each $N^Z(E)$ curve, an energy E^N_{max} where $N^Z(E)$ achieves its maximum is indicated by a vertical arrow.(*F*) Plot of measured $E^N_{max}(p)$ for $P = 0.06, 0.08, 0.10, 0.14$, and 0.17. This shows how the energy associated with maximum spectral intensity of the NE state diminishes approximately linearly with increasing p.

at bias voltage $V = E/e$ and with spatial resolution of typically 7×7 pixels within each CuO_2 unit cell. To suppress serious systematic "set-point" errors (33) we evaluate $Z(\boldsymbol{r}, E) = g(\boldsymbol{r}, E)/g(\boldsymbol{r}, -E)$, a function for which distances, wavelengths, spatial phases, and energy magnitudes of electronic structure can be measured accurately. The necessary spatial-phase accuracy in $g(\boldsymbol{r}, E)$ and $Z(\boldsymbol{r}, E)$ is achieved using a picometer-scale transformation that renders the topographic image $T(\boldsymbol{r})$ perfectly a_0-periodic, and is then applied to $g(\boldsymbol{r}, E)$ to register all of the electronic-structure data to the ideal CuO_2 lattice (8, 28–30). The necessity of these advanced SI-STM techniques to measure the cuprate broken-symmetry phases can be seen directly in Fig. 2*A* which shows a typical $Z(\boldsymbol{r}, E)$, with local breaking of C_4 symmetry within the CuO_2 cell (NE) and its periodic modulations (DW); a schematic overlay is used to identify the locations of Cu and O orbitals. Fig. 2*B* is the Fourier transform of a larger-FOV $Z(\boldsymbol{r}, E \sim 100\ \text{meV})$ image of $Bi_2Sr_2CaCu_2O_{8+x}$ at $p \sim 0.06$ containing the two basic signatures of electronic symmetry breaking, the Bragg peaks at $\boldsymbol{Q}^B = ((1,0)(0,1))2\pi/a_0$ and the peaks near $\boldsymbol{Q}^D \approx ((0.75,0)(0,0.75))2\pi/a_0$ due to the *d*-symmetry form factor DW (28–30).

The $\boldsymbol{Q} = 0$ rotational symmetry-breaking state (NE) is detected by resolving both the real $ReZ(\boldsymbol{Q}^B, E)$ and imaginary $ImZ(\boldsymbol{Q}^B, E)$ components of the Bragg amplitudes of $Z(\boldsymbol{q}, E)$, to form a direct measure of intraunit cell nematicity (8)

$$N^Z(E) \equiv ReZ\left(\boldsymbol{Q}_y^B, E\right) - ReZ(\boldsymbol{Q}_x^B, E), \qquad [1]$$

where $\boldsymbol{Q}_y^B$ and $\boldsymbol{Q}_x^B$ are the two Bragg wavevectors along the y axis/x axis, respectively. Any spurious effects of STM tip anisotropy on $N^Z(E)$ are ruled out as described in *SI Appendix*, section 1. If the measured $N^Z(E)$ is then nonzero, breaking of C_4 symmetry is occurring due to inequivalence on the average of electronic structure at the two oxygen sites within each CuO_2 cell (8, 28–33). Fig. 3 *A–E* shows the measured energy dependence of $ReZ(\boldsymbol{Q}_y^B, E), ReZ(\boldsymbol{Q}_x^B, E)$, and their difference $N^Z(E)$ for $Bi_2Sr_2CaCu_2O_{8+x}$ at $P = 0.06, 0.08, 0.10, 0.14$, and 0.17. Fig. 3*F* then summarizes the doping dependence of the energy, E^N_{max}, at which $N^Z(E)$ achieves its maximum intensity. Thus, the characteristic energy of maximum spectral intensity of this measure of cuprate nematicity diminishes approximately linearly with increasing p.

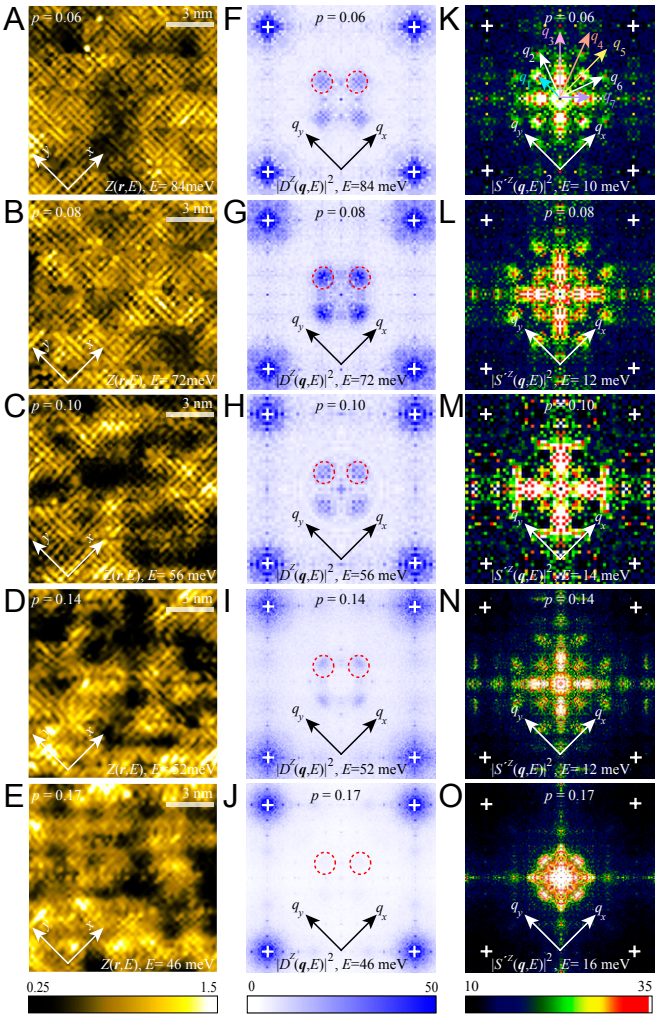

Fig. 4. Doping evolution of the $Q \neq 0$ broken-symmetry (DW) state. (*A–E*) Real-space map of phase-resolved DW modulations in $Z(\boldsymbol{r}, E)$ measured at $T = 2.2$ K for doping $P = 0.06, 0.08, 0.10, 0.14$, and 0.17 at $E = 84, 72, 56, 52$, and 46 meV, respectively. (*F–J*) Corresponding q-space DW power-spectral densities $|D^Z(\boldsymbol{q}, E)|^2$ from Eq. **2** for dopings $P = 0.06, 0.08, 0.10, 0.14$, and 0.17, respectively. Red circles represent the relevant regions of interest for *d*FF DW at wavevectors $\boldsymbol{Q}^D \cong ((0.25,0)(0,0.25))2\pi/a_0$. Locations of the Bragg peaks Q_x^B, Q_y^B are indicated by "+" sign. (*K–O*) The power-spectral densities of Bogoliubov quasiparticle $|S'^Z(\boldsymbol{q}, E)|^2$ from Eq. **2** for dopings $P = 0.06, 0.08, 0.10, 0.14$ and 0.17, respectively, measured at lower energy on the same sample set. Locations of the Bragg peaks Q_x^B, Q_y^B are indicated by "+" sign.

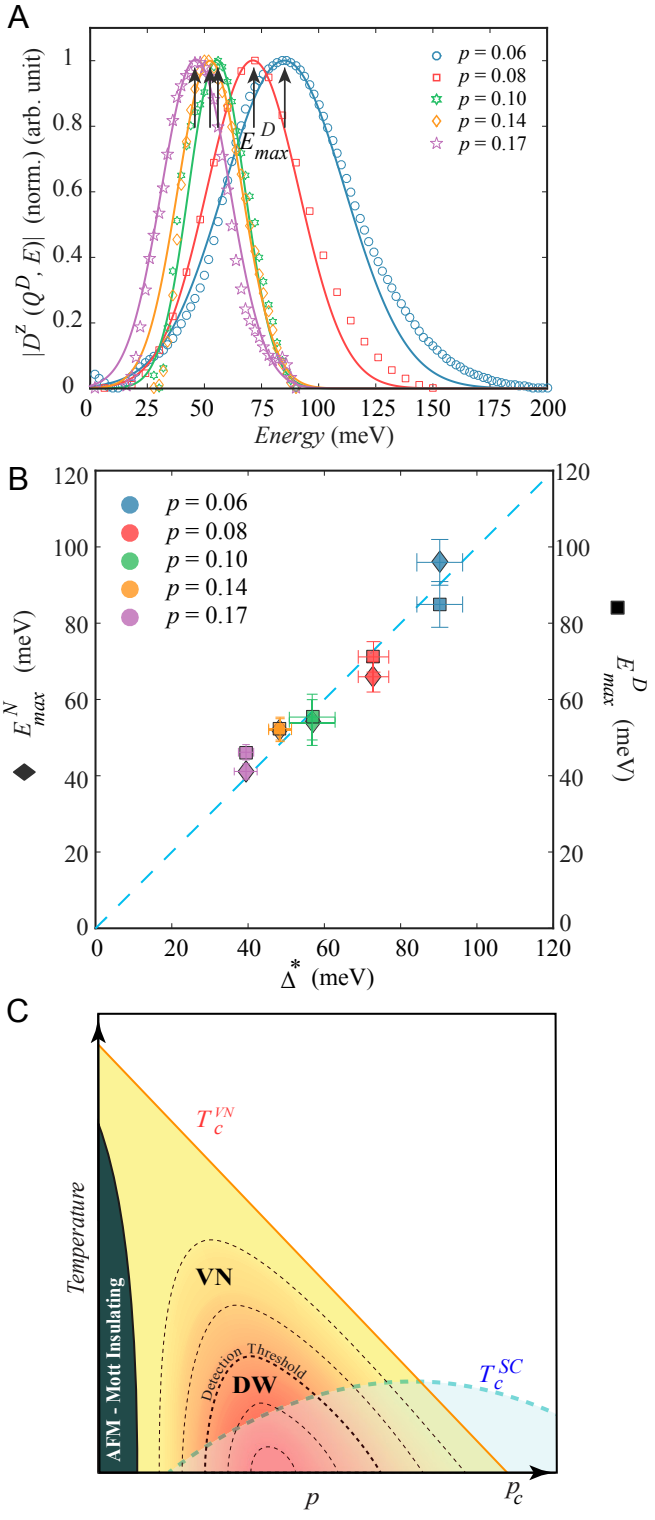

Fig. 5. Relationship of characteristic energies of NE, DW states, and the PG. (*A*) Measured energy variation of normalized amplitude for *d*FF DW versus doping. The corresponding Gaussian fit to the data, used to extract the peak positions, is shown in solid curves. The *d*FF DW amplitude is extracted by integrating $|D^Z(\boldsymbol{q},E)|^2$ over the primary DW wavevectors at $\boldsymbol{Q}^D \cong ((0.25,0)(0,0.25))2\pi/a_0$ (red circles in Fig. 4 *F–J*). The data for hole density $p = 0.06$, 0.08, 0.10, 0.14, and 0.17 in the $Bi_2Sr_2CaCu_2O_{8+\delta}$ samples are reported here. For each $|D^Z(\boldsymbol{q},E)|^2$ curve, an energy E^D_{max} for maximum spectral weight is indicated by a vertical arrow. (*B*) Plot of measured $E^N_{max}(p)$ *and* $E^D_{max}(p)$ versus $\Delta^*(p)$ for values of $p = 0.06$, 0.08, 0.10, 0.14, and 0.17. This shows how the energy for maximum spectral intensity of both the NE and the DW states diminishes approximately linearly with increasing p, and that they are always virtually identical to each other and to the PG energy. Dashed blue line is a guide to the eye. (*C*) A schematic diagram of the hypothesized VN state within the cuprate phase diagram (37). The VN hypothesis appears consistent with all of the data and analysis presented throughout this paper. Note that the antiferromagnetic Mott insulator and superconducting regions shown here are not included in the analysis of refs. 37 and 38.

The translational symmetry-breaking (DW) state exhibits a predominantly *d*-symmetry form factor (*d*FF) because the DW is based on modulating the inequivalence between the O_x and O_y sites within each CuO_2 unit cell (8, 28–33) at wavevector $\boldsymbol{Q}^D_x$, as discussed in *SI Appendix*, section 2. Such modulations are described by $A(\boldsymbol{r}) = D(\boldsymbol{r})Cos(\phi(\boldsymbol{r}) + \phi_0(\mathbf{r}))$, where $\phi(\boldsymbol{r}) = \boldsymbol{Q}^D_x \cdot \boldsymbol{r}$ is the DW spatial phase at location $\boldsymbol{r}$ and $D(\boldsymbol{r})$ is the magnitude of the *d*FF. $D(\boldsymbol{r}) = A_D$ when $r = r_{O_x}$, $D(\boldsymbol{r}) = -A_D$ when $r = r_{O_y}$, and $D(\boldsymbol{r}) = 0$ otherwise, where A_D is a real number for the amplitude. To study this state, the sublattice-phase-resolved $Z(\boldsymbol{r},E)$ images are separated into three: $Cu(\boldsymbol{r})$, containing only Cu sites, and $O_x(\boldsymbol{r})$; $O_y(\boldsymbol{r})$, containing only the *x*/*y* axis oxygen sites. Phase-resolved Fourier transforms of the $O_x(\boldsymbol{r},E)$ and $O_y(\boldsymbol{r},E)$ sublattice images, $\tilde{O}_x(\boldsymbol{q},E) = Re\tilde{O}_x(\boldsymbol{q},E) + iIm\tilde{O}_x(\boldsymbol{q},E)$; $\tilde{O}_y(\boldsymbol{q},E) = Re\tilde{O}_y(\boldsymbol{q},E) + iIm\tilde{O}_y(\boldsymbol{q},E)$, are then used to determine the FF symmetry for modulations at any $\boldsymbol{q}$

$$D^Z(\boldsymbol{q},E) = \left(\tilde{O}_x(\boldsymbol{q},E) - \tilde{O}_y(\boldsymbol{q},E)\right), \qquad \textbf{[2a]}$$

$$S^{'Z}(\boldsymbol{q},E) = \left(\tilde{O}_x(\boldsymbol{q},E) + \tilde{O}_y(\boldsymbol{q},E)\right). \qquad \textbf{[2b]}$$

Fig. 4 *A–E* show our typical images of $Z(\boldsymbol{r},E \sim \Delta^*)$ while Fig. 4 *F–J* show $|D^Z(\boldsymbol{q},E \sim \Delta^*)|^2$ the *d*FF, power spectral density Fourier transforms derived from Fig. 4 *A–E*. The peaks identified by red dashed circles are the signature of the *d*FF DW state (28–32). At atomic scale, these features in $D^Z(\boldsymbol{q},E \sim \Delta^*)$ represent two populations of nanoscale unidirectional *d*FF DW domains (29).

Evolution of Broken-Symmetry Spectral Weight with Hole Density. Our second key objective is then to measure the doping dependence of the energy, E^D_{max}, at which the DW order $D^Z(\boldsymbol{Q}^D,E)$ achieves its maximum spectral intensity. Fig. 5*A* shows the measured $|D^Z(\boldsymbol{Q}^D,E)|$ integrated within the dashed circles in Fig. 4 *F–J* for $P = 0.6$, 0.8, 0.10, 0.14, and 0.17 plotted versus energy E. The *dFF* is negligible for modulations in the low-energy range of Bogoliubov quasiparticles (Fig. 4 *K–O*), but $D^Z(\boldsymbol{Q}^D,E)$ rapidly becomes intense at higher energy before finally diminishing quickly at highest E. Evidently, for each p there is a specific energy E^D_{max} at which a maximum in $|D^Z(\boldsymbol{Q}^D,E)|$ occurs. The values of E^D_{max} are indicated by the black arrows in Fig. 5*A*, and these we associate with the energy gaps of the disordered DW (*SI Appendix*, section 3). Fig. 5*B* then summarizes the doping dependence of measured E^D_{max}, revealing that that the characteristic energy of maximum spectral intensity of the DW state also diminishes approximately linearly with increasing p.

To appreciate the implications of these observations, it is important to realize that the order parameters $N^Z(E)$ in Eq. **1** and $D^Z(\boldsymbol{q},E)$ in Eq. **2a** use no common $\boldsymbol{q}$-space data whatsoever, despite having been measured in the identical real-space field of view. The key experimental result of these studies is then shown in Fig. 5*B*: a combined plot of measured $E^N_{max}(p)$, $E^D_{max}(p)$ versus the measured values of $\Delta^*(p)$ for underdoped $Bi_2Sr_2CaCu_2O_{8+x}$ samples with $0.06 \le p \le 0.17$.The striking fact it reveals is that the two characteristic energies E^N_{max} and E^D_{max}, where the distinct

broken-symmetry states NE and DW have maximal spectral intensity, are indistinguishable from each other throughout this wide region of the underdoped phase diagram. Even more notably, both $E^N_{max}(p)$ and $E^D_{max}(p)$ follow a trajectory with doping that is indistinguishable within error bars from that of the independently measured pseudogap energy $\Delta^*(p)$ (Fig. 1 *A* and *B*). Therefore, we find that the characteristic energy of maximal spectral intensity for both cuprate broken-symmetry states is always the pseudogap energy $\Delta^*(p)$. These results add yet another conundrum to our list: How could the characteristic energies of NE and DW states be virtually identical to each other and to the PG energy Δ^* (Fig. 5*B*) over this wide range of doping, while the onset temperatures $T_{NE}(p)$ and $T_{DW}(p)$ of these phases appear unrelated to each other and to vary quite differently with doping (Fig. 1*C*)? Combined with the question of why the DW state (which should generate an energy gap) appears without any new gap opening at $T_{DW}(p)$, while the NE state (which should be incapable of opening an energy gap) emerges at the pseudogap opening temperature $T_{NE}(p) \approx T^*(p)$ (Fig. 1*C*), presents an intricate puzzle.

Analysis. In pursuit of its resolution, we note that electronic liquid crystal states of a doped Mott insulator are naturally expected to exhibit distinct NE and DW broken-symmetry phases (34–36). Within this context, the critical temperatures and characteristic electronic energies of these two highly distinct phases are not required to be related, except for the fact that the NE phase should appear first with falling temperature. Recently, however, the effects of quenched disorder on the quasi-2D version of this situation have been discovered (37, 38). The remarkable conclusion is that, while long-range order of a unidirectional incommensurate finite-$\boldsymbol{Q}$ DW cannot exist in the presence of quenched disorder, its short-range relict survives up to a certain critical disorder strength but in the form of a $\boldsymbol{Q} = 0$ broken rotational-symmetry state. This state was dubbed a vestigial nematic (37, 38) (VN). Note that, as with the unidirectional *s*-symmetry FF DW state considered in ref. 37, a unidirectional *d*FF DW state (as in underdoped cuprates) also breaks local translational and rotational symmetries (28–30), and should also yield a VN state in the presence of strong disorder. Several distinguishing consequences are predicted within such VN theories. First, the energy scale of the NE state for which rotational symmetry is broken globally should always be the same as that of the DW state in which translational symmetry is broken locally, since the two effects stem from the identical microscopic electronic phenomenon (unidirectional DW with disorder). Second, as temperature diminishes below the phase transition where the VN state appears and its gap opens, the intensity of the short-range DW underpinning the VN should increase continuously as thermal fluctuations are reduced but with no new phase transition and no additional gap opening, as indicated schematically by dashed contours in Fig. 5*C*. Here, the horizontal axis is carrier density but, because strong spatial correlations exist between dopant atom distributions and electronic disorder in $Bi_2Sr_2CaCu_2O_{8+x}$ (39), it also corresponds with disorder strength (37, 38) for that material.

VN theories cast a fresh light on the perplexing phenomenology of the NE (3–16) and DW (17–27) symmetry breaking in the cuprate pseudogap phase (Figs. 2–5). If this phase is a VN state, then a highly disordered DW opens a gap Δ^* at T^* but without long-range DW order, so that only a VN phase appears. The VN model then implies that all three energies: the pseudogap, the characteristic energy gap of the DW, and the apparent energy gap of the NE state, should all coincide at every doping. This is because all three signatures derive from the same microscopic phenomenon: the appearance of the unidirectional but disordered DW state. Coincidence of measured $E^N_{max}(p)$, $E^D_{max}(p)$, and $\Delta^*(p)$ is precisely what we report in Fig. 5*B*, for underdoped $Bi_2Sr_2CaCu_2O_{8+x}$ samples over a wide doping range $0.06 \le p \le 0.17$. Moreover, in a VN state with phase transition at $T_{NE}(p)$, the onset temperatures $T_{NE}(p)$ and $T_{DW}(p)$ should be unrelated to each other and vary independently with doping, provided $T_{DW}(p)$ is an instrumentation-limited threshold for detection of the disordered charge modulations rather than a phase transition. In that case, detection of DW phenomena should not coincide with opening of a new gap at $T_{DW}(p)$ because the DW gap has already opened at $T_{NE}(p) \approx T^*(p)$ when the VN phase transition occurs. Thus, VN theory (37, 38) appears highly consistent with the experimental observations reported herein (Fig. 5*B*), and more generally with the intricate phenomenology of thermal transitions, energy-gap opening, and distinct symmetry breaking in underdoped cuprates (3–32) (Fig. 1*C*). We note, however, that neither VN theory nor our studies here yet discriminate whether the fundamental DW state with wavevector $\boldsymbol{Q}$ is a conventional charge-DW with order parameter $\langle c^\dagger_k c_{k+Q}\rangle$ or is a pair-DW (40) with order parameter $\left\langle c^\dagger_k c^\dagger_{-k+Q}\right\rangle$.

ACKNOWLEDGMENTS. S.M. acknowledges support from NSF Grant DMR-1719875 to the Cornell Center for Materials Research. S.-i.U. and H.E. acknowledge support from a Grant-in-Aid for Scientific Research from the Ministry of Science and Education (Japan) and the Global Centers of Excellence Program for Japan Society for the Promotion of Science. K.F. and C.K.K. acknowledge salary support from the US Department of Energy, Office of Basic Energy Sciences, under Contract DEAC02-98CH10886. E.-A.K. acknowledges Simons Fellow in Theoretical Physics Award 392182 and from the US Department of Energy, Office of Basic Energy Sciences, under Grant DE-SC0018946. S.D.E. acknowledges studentship funding from the Engineering and Physical Sciences Research Council under Grant EP/G03673X/1. M.H.H., S.D.E., and J.C.S.D. acknowledge support from the Gordon and Betty Moore Foundation's EPiQS Initiative through Grant GBMF4544. J.C.S.D. acknowledges support from Science Foundation Ireland under Award SFI 17/RP/5445 and from the European Research Council under Award DLV-788932.

1. J. L. Tallon, J. W. Loram, The doping dependence of *T**–What is the real high-T_c phase diagram? *Physica C* **349**, 53–68 (2001).
2. M. R. Norman, D. Pines, C. Kallin, The pseudogap: Friend or foe of high Tc? *Adv. Phys.* **54**, 715–733 (2005).
3. A. Kaminski *et al*., Spontaneous breaking of time-reversal symmetry in the pseudogap state of a high-T_c superconductor. *Nature* **416**, 610–613 (2002).
4. B. Fauqué *et al*., Magnetic order in the pseudogap phase of high-T_c superconductors. *Phys. Rev. Lett.* **96**, 197001 (2006).
5. H. A. Mook, Y. Sidis, B. Fauqué, V. Balédent, P. Bourges, Observation of magnetic order in a superconducting $YBa_2Cu_3O_{6.6}$ single crystal using polarized neutron scattering. *Phys. Rev. B Condens. Matter Mater. Phys.* **78**, 020506(R) (2008).
6. Y. Li *et al*., Unusual magnetic order in the pseudogap region of the superconductor $HgBa_2CuO_{4+\delta}$. *Nature* **455**, 372–375 (2008).
7. J. Xia *et al*., Polar Kerr-effect measurements of the high-temperature $YBa_2Cu_3O_{6+x}$ superconductor: Evidence for broken symmetry near the pseudogap temperature. *Phys. Rev. Lett.* **100**, 127002 (2008).
8. M. J. Lawler *et al*., Intra-unit-cell electronic nematicity of the high-T_c copper-oxide pseudogap states. *Nature* **466**, 347–351 (2010).
9. R.-H. He *et al*., From a single-band metal to a high-temperature superconductor via two thermal phase transitions. *Science* **331**, 1579–1583 (2011).
10. Y. Li *et al*., Magnetic order in the pseudogap phase of $HgBa_2CuO_{4+\delta}$ studied by spin-polarized neutron diffraction. *Phys. Rev. B Condens. Matter Mater. Phys.* **84**, 224508 (2011).
11. A. Shekhter *et al*., Bounding the pseudogap with a line of phase transitions in $YBa_2Cu_3O_{6+\delta}$. *Nature* **498**, 75–77 (2013).
12. L. Zhao *et al*., A global inversion-symmetry-broken phase inside the pseudogap region of $YBa_2Cu_3O_y$. *Nat. Phys.* **13**, 250–254 (2017).
13. L. Mangin-Thro, Y. Sidis, A. Wildes, P. Bourges, Intra-unit-cell magnetic correlations near optimal doping in YBa2Cu3O6.85. *Nat Commun* **6**, 7705 (2015).
14. L. Mangin-Thro, Y. Li, Y. Sidis, P. Bourges, a–b anisotropy of the intra-unit-cell magnetic order in $YBa_2Cu_3O_{6.6}$. *Phys. Rev. Lett.* **118**, 097003 (2017).
15. Y. Sato *et al*., Thermodynamic evidence for a nematic phase transition at the onset of the pseudogap in $YBa_2Cu_3O_y$. *Nat. Phys.* **13**, 1074–1078 (2017).
16. S. Nakata, *et al*., Nematicity in the pseudogap state of cuprate superconductors revealed by ARPES. arxiv 1811.10028. Accessed 5 December 2018.
17. J. M. Tranquada, B. J. Sternlieb, J. D. Axe, Y. Nakamura, S. Uchida, Evidence for stripe correlations of spins and holes in copper oxide superconductors. *Nature* **375**, 561–563 (1995).
18. M. Hücker *et al*., Stripe order in superconducting $La_{2-x}Ba_xCuO_4$ ($0.095 \le x \le 0.155$). *Phys. Rev. B Condens. Matter Mater. Phys.* **83**, 104506-1–104506-16 (2011).
19. Y. J. Kim, G. D. Gu, T. Gog, D. Casa, X-ray scattering study of charge density waves in $La_{2-x}Ba_xCuO_4$. *Phys. Rev. B Condens. Matter Mater. Phys.* **77**, 064520 (2008).

20. J. Chang *et al*., Direct observation of competition between superconductivity and charge density wave order in $YBa_2Cu_3O_{6.67}$. *Nat. Phys.* **8**, 871–876 (2012).
21. G. Ghiringhelli *et al*., Long-range incommensurate charge fluctuations in $(Y,Nd)Ba_2Cu_3O_{(6+x)}$. *Science* **337**, 821–825 (2012).
22. A. J. Achkar *et al*., Distinct charge orders in the planes and chains of ortho-III-ordered $YBa_2Cu_3O_{(6+\delta)}$ superconductors identified by resonant elastic x-ray scattering. *Phys. Rev. Lett.* **109**, 167001 (2012).
23. E. Blackburn *et al*., X-ray diffraction observations of a charge-density-wave order in superconducting ortho-II $YBa_2Cu_3O_{6.54}$ single crystals in zero magnetic field. *Phys. Rev. Lett.* **110**, 137004 (2013).
24. R. Comin *et al*., Charge order driven by Fermi-arc instability in $Bi_2Sr_{(2-x)}La_{(x)}CuO_{(6+\delta)}$. *Science* **343**, 390–392 (2014).
25. S. Blanco-Canosa *et al*., Resonant x-ray scattering study of charge-density wave correlations in $YBa_2Cu_3O_{6+x}$. *Phys. Rev. B Condens. Matter Mater. Phys.* **90**, 054513 (2014).
26. S. Gerber *et al*., Three-dimensional charge density wave order in $YBa_2Cu_3O_{6.67}$ at high magnetic fields. *Science* **350**, 949–952 (2015).
27. G. Campi *et al*., Inhomogeneity of charge-density-wave order and quenched disorder in a high-Tc superconductor. *Nature* **525**, 359–362 (2015).
28. K. Fujita *et al*., Direct phase-sensitive identification of a *d*-form factor density wave in underdoped cuprates. *Proc. Natl. Acad. Sci. U.S.A.* **111**, E3026–E3032 (2014).
29. M. H. Hamidian *et al*., Atomic-scale electronic structure of the cuprate *d*-symmetry form factor density wave state. *Nat. Phys.* **12**, 150–156 (2016).
30. A. Mesaros *et al*., Topological defects coupling smectic modulations to intra-unit-cell nematicity in cuprates. *Science* **333**, 426–430 (2011).
31. R. Comin *et al*., Symmetry of charge order in cuprates. *Nat. Mater.* **14**, 796–800 (2015).
32. E. M. Forgan *et al*., The microscopic structure of charge density waves in underdoped YBa2Cu3O6.54 revealed by X-ray diffraction. *Nat Commun* **6**, 10064 (2015).
33. K. Fujita *et al*., Spectroscopic imaging scanning tunneling microscopy studies of electronic structure in the superconducting and pseudogap phases of cuprate high-T_c superconductors. *J. Phys. Soc. Jpn.* **81**, 011005 (2011).
34. S. A. Kivelson, E. Fradkin, V. J. Emery, Electronic liquid-crystal phases of a doped Mott insulator. *Nature* **393**, 550–553 (1998).
35. V. J. Emery, S. A. Kivelson, J. M. Tranquada, Stripe phases in high-temperature superconductors. *Proc. Natl. Acad. Sci. U.S.A.* **96**, 8814–8817 (1999).
36. E. Fradkin, S. A. Kivelson, J. M. Tranquada, Colloquium: Theory of intertwined orders in HTSC. *Rev. Mod. Phys.* **87**, 457–482 (2015).
37. L. Nie, G. Tarjus, S. A. Kivelson, Quenched disorder and vestigial nematicity in the pseudogap regime of the cuprates. *Proc. Natl. Acad. Sci. U.S.A.* **111**, 7980–7985 (2014).
38. L. Nie, A. V. Maharaj, E. Fradkin, S. A. Kivelson, Vestigial nematicity from spin and/or charge order in the cuprates. *Phys. Rev. B* **96**, 085142 (2017).
39. K. McElroy *et al*., Atomic-scale sources and mechanism of nanoscale electronic-disorder in $Bi_2Sr_2CaCu_2O_{8+\delta}$. *Science* **309**, 1048–1052 (2005).
40. M. H. Hamidian *et al*., Detection of a Cooper-pair density wave in Bi2Sr2CaCu2O8+x. *Nature* **532**, 343–347 (2016).